The nontraditional Coriolis terms and convective system propagation

Hing Ong [a] and Da Yang [a,b]

[a] *University of California, Davis, Davis, CA*

[b] *Lawrence Berkeley National Laboratory, Berkeley, CA*

Corresponding author: Hing Ong, hxong@ucdavis.edu

This work has been submitted to *J. Atmos. Sci.* Copyright in this work may be transferred without further notice.

ABSTRACT

This study explores effects of the nontraditional Coriolis terms (NCTs) on convective system propagation in radiative-convective equilibrium (RCE). NCTs are restored to the System for Atmospheric Modeling (SAM) to explicitly simulate the temporal evolution of convective systems in a zonal vertical domain rotating about a meridional axis. The system rotation rate is tested over a wide range. The results are transformed into space-time spectra to analyze the overall propagation characteristics. The raw spectra show local power maxima in bands associated with self-aggregated convection and convectively coupled gravity waves. Changes in the spectra due to the inclusion of NCTs can mostly be explained by the compressional beta effect (CBE), which tends to transmit zonal vertical circulation eastward. For example, the spectral power increases in the band of eastward propagating convective clusters and decreases in the band of westward ones. Furthermore, the speed changes of convectively coupled gravity waves are measured from the spectra. The results suggest that the inclusion of NCTs speeds up the eastward propagation and slows down the westward propagation. The magnitude of the speed changes increases with the system rotation rate, and this increase agrees with the theoretical speed change due to the CBE. These changes are robust and considerable to a far larger extent than the computational cost for the implementation of NCTs in SAM. Thus, this study reconfirms that the restoration of NCTs is economical for model development.

SIGNIFICANCE STATEMENT

The rotation of Earth turns eastward motion upward and upward motion westward, and vice versa. This effect is called the nontraditional Coriolis effect and is omitted in most of the current atmospheric models for predicting weather and climate. Using an idealized model with cloud physics, this study suggests that the inclusion of the nontraditional Coriolis effect speeds up eastward moving rainy systems and slows down westward moving ones. The speed change agrees with a theory without cloud physics. This study encourages restoring the nontraditional Coriolis effect to the atmospheric models since its increase in the accuracy of tropical large-scale weather prediction is far larger than its increase in the cost.

1. Introduction

Most global weather and climate models solve the primitive equations for Earth's atmosphere, assuming a thin atmosphere in the hydrostatic balance. To conserve energy and angular momentum, these models neglect the locally horizontal component of the Earth's rotation vector. This is called the traditional approximation (Eckart 1960), and the neglected Coriolis components are known as the nontraditional Coriolis terms (NCTs). These approximations were believed to hold accurately for large-scale circulations in Earth's atmosphere (e.g., Vallis 2017).

However, recent studies discovered that NCTs can significantly affect thermodynamic states and atmospheric circulations in the tropics (M. Hayashi and Itoh 2012; Igel and Biello 2020; Ong and Roundy 2019, 2020a, 2020b). For example, NCTs affect thickness between pressure levels—a measure of effective atmospheric buoyancy—by about 10% of the thickness variability (Ong and Roundy 2020a). Ong and Roundy (2019) found that, in response to steady heat sources, NCTs can generate anomalous winds that are about 12% of the total wind response. Ong and Roundy (2020b, hereafter OR20b) further showed that NCTs produce a significant eastward propagation tendency for atmospheric waves in Earth's tropics. The underlying mechanism was the compressional beta effect (CBE), which had been only considered significant in the atmosphere of giant planets and stars (e.g., Gilman and Glatzmaier 1981; Glatzmaier et al. 2009; Verhoeven and Stellmach 2014).

These recent studies have advanced our understanding of NCTs. However, most of them were based on simple models with imposed flow field or prescribed moist physics and solved linear problems. This study uses a zonal vertical two-dimensional (2D) nonlinear cloud-resolving model (CRM) to further explore possible effects of NCTs on explicitly simulated convectively coupled circulations. The 2D CRM experiments simulate gravity waves and self-

aggregated convection (e.g., Held et al. 1993; Yang 2018) in radiative-convective equilibrium (RCE), and their propagation characteristics are examined given NCTs switched on and off.

The rest of this paper is organized as follows. Section 2 reviews the CBE and forms a hypothesis. Section 3 describes the methods of modeling and spectral analyses. Section 4 presents the results and tests the hypothesis. Section 5 summarizes this paper and discusses the implications for the Madden–Julian oscillation (MJO).

2. The Compressional Beta Effect (CBE)

OR20b introduced both NCTs and the vertically decreasing density to the wave theory on an equatorial beta plane (Matsuno 1966). This study confines the domain to a zonal vertical plane at the equator, so all the wave modes degenerate except one mode originally associated with the Kelvin waves. The remaining mode becomes associated with gravity waves modified by the CBE propagating either westward or eastward; the original reason no longer applies for discarding the westward part. Without the CBE, the gravity wave mode would be west-east symmetric. Modified by the CBE, the dispersion relation of gravity waves can be approximated to the first order as follows. Start from rearranging equation (11) of OR20b and taking the quasi-hydrostatic approximation:

$$c^2 - \frac{2\Omega}{{m_H}^2 H} c - \frac{\widetilde{N}^2}{{m_H}^2} = 0, \tag{1}$$

where the variables are defined as follows: c, phase speed; Ω, planetary or system rotation rate; H, scale height; $\widetilde{N}$, effective buoyancy frequency; ${m_H}^2 \equiv m^2 + 1/(4H^2)$, where m denotes vertical wavenumber. Solve Eq. (1) for c:

$$c = \frac{\Omega}{{m_H}^2 H} \pm \frac{\widetilde{N}}{m_H} \sqrt{1 + \left(\frac{\Omega}{{m_H}^2 H} \frac{m_H}{\widetilde{N}} \right)^2}. \tag{2}$$

Define $c_0 \equiv c(\Omega = 0) = \pm \widetilde{N}/m_H$ and rewrite Eq. (2):

$$c = \frac{\Omega}{{m_H}^2 H} + c_0\sqrt{1 + \left(\frac{\Omega}{{m_H}^2 H c_0}\right)^2}. \quad (3)$$

Using $\hat{c} \equiv c/c_0$ and $\hat{\Omega} \equiv \Omega/({m_H}^2 H c_0)$, nondimensionalize Eq. (3):

$$\hat{c} = \hat{\Omega} + \sqrt{1 + \hat{\Omega}^2}. \quad (4)$$

Expand the square root in Eq. (4) around $\hat{\Omega}^2 = 0$:

$$\hat{c} = 1 + \hat{\Omega} + \frac{\hat{\Omega}^2}{2} + O\left(\hat{\Omega}^4\right). \quad (5)$$

Define $\Delta c \equiv c - c_0$ and dimensionalize Eq. (5):

$$\Delta c = \frac{\Omega}{{m_H}^2 H} + \frac{1}{2c_0}\left(\frac{\Omega}{{m_H}^2 H}\right)^2 + c_0 O\left(\hat{\Omega}^4\right). \quad (6)$$

The first term on the right-hand side is defined as the first-order CBE (FOCBE) parameter. A negative phase speed denotes westward propagation, and vice versa. Figure 1 depicts three pairs of c and c_0 in a wavenumber-frequency domain given the FOCBE parameter in the tropical troposphere derived from an observational dataset (see Section 4 for estimation), and it shows that the FOCBE makes gravity waves propagate faster eastward and slower westward in a way that the dispersion lines rotate counterclockwise in the wavenumber-frequency domain. The higher-order terms are negligible since $\hat{\Omega}$ is small in general; for example, the three pairs of c_0 in Figure 1 correspond to $\hat{\Omega}$ of 1/6, 1/18, and 1/54 (from slow to fast).

3. Methods

a. Model Description

This study uses the System for Atmospheric Modeling (SAM) (Khairoutdinov and Randall 2003) version 6.11.2 and complies with the protocol of RCE Model Intercomparison Project (RCEMIP; Wing et al. 2018, 2020). We restored NCTs to SAM as released in version 6.11.7.

The implementation of NCTs was validated by the compressional Rossby wave benchmark (OR20b). It increases the central processing unit (CPU) time by less than 0.01% of the total cost of full-physics simulations. Thus, the cost for NCTs is negligible. This is consistent with Skamarock et al. (2021), who reported that the restoration of NCTs increases the cost of the global atmospheric dynamical core by less than 5%.

Deviations from the RCEMIP protocol (Wing et al. 2018) are explained as follows. First, six simulations are conducted with the system rotation rate set to 0, 1, 4, 8, 16, and 64 times the Earth's rotation rate (named X00, X01, X04, X08, X16, and X64). Second, the meridional dimension is eliminated (2D). Third, the size of the zonal and temporal dimensions is 24,576 km and 1,632 Earth's days. Fourth, the model top is lowered from 33 km to 28 km. Last, mean zonal velocity is nudged toward zero at each level.

All other procedures and settings follow the elongated channel SAM simulation over sea surface temperature of 300 K in RCEMIP (labeled SAM_CRM/RCE_large300). The initial vertical profile is derived from the corresponding small domain simulation data in RCEMIP (labeled SAM_CRM/RCE_small300). In theory, the X00 spectrum should be west-east symmetric.

b. Spectral Analyses

To analyze the overall propagation characteristics of convective systems in the 2D RCE simulations, the data except the first 96 days are transformed into space-time spectra mostly following the sampling procedure by Wheeler and Kiladis (1999, hereafter WK99) based on the method by Y. Hayashi (1971, 1982). The sample length is 64 days. This procedure yields raw spectral power in the wavenumber-frequency domain. To focus on the east-west asymmetry, we contrast the raw spectra to reference spectra made from the X00 spectra by taking the average of spectral power density symmetric about wavenumber zero.

To measure the gravity wave speed, we take the power-weighted average of phase speed in a gravity wave band. We determine gravity wave bands mostly using the normalization procedure by WK99. To quantify the uncertainty, we test the sample lengths of 128, 192, 256, 384, 512, and 768 days, and the smoothing passes in wavenumber of 16, 32, 48, and 64 times. The smoothing passes in frequency are set to the sample length divided by 8.

To estimate the vertical wavenumber relevant to the FOCBE parameter, the data are transformed into vertical normal modes assuming a rigid tropopause (Fulton and Schubert 1985) with the approximated set of analytic basis functions omitting small vertical variations of scale height and static stability (Kiladis et al. 2009) as follows:

$$\sqrt{\rho(z)}u(x,z,t) = \sum_{M=0}^{\infty} U_M(x,t)\cos\left(\frac{M\pi z}{D}\right), z \in [0,D], \quad (7)$$

where the variables are defined as follows: ρ, density; u, zonal velocity; D, tropopause height; and U_M, amplitude of the Mth vertical mode. The vertical wavenumber m equals to $M\pi/D$. The power ${U_M}^2$ is proportional to the vertically integrated kinetic energy of the vertical mode. Given the level of the minimum temperature in the mean profile, D is located at 15.5 km. The data are linearly interpolated to vertical levels equally spaced by $\Delta z = 500$ m from $\Delta z/2$ to $D - \Delta z/2$, and then $\sqrt{\rho}u$ is calculated. Then, the domain is extended to $2D - \Delta z/2$, and the upper half of the new domain is filled with the mirror image of $\sqrt{\rho}u$ from the lower half. For each profile, a fast Fourier transform is performed. The resulting coefficients can be filtered for a target timescale with the Lanczos filter. This procedure yields the vertical-mode spectrum.

For comparison, the same vertical-mode analysis is applied to an observational dataset. The dataset used is the Merged Sounding (Giangrande et al. 2011) over Gan Island, Maldives from 1 October 2011 to 9 February 2012 during the Dynamics of the MJO (DYNAMO) field

campaign (Yoneyama et al. 2013). The above-mentioned procedure is followed, but D and Δz are 17.0 km and 200 m.

4. Results

We first focus on the raw spectra without NCTs (top row of Figure 2) of precipitation rate, precipitable water (PW), zonal velocity at the lowest level (USFC) and at 200 hPa (U200). They all show power peaks associated with convectively coupled gravity waves with a speed of about ±16 m s^{-1} (dotted lines: 26-m equivalent depth). In addition, they show peaks corresponding to dry gravity waves with a speed of about ±42 m s^{-1} (solid lines: 180-m equivalent depth) except in the precipitation spectrum (Figure 2a). Moreover, they show another pair of local power maxima at the lowest resolved frequency at around wavenumber ±12 except in the U200 spectrum (Figure 2d). These low-frequency spectral peaks correspond to slowly propagating long-lived convective systems with a characteristic wavelength of 2,048 km, which conforms to the scale of the self-aggregated convective clusters in Yang's (2018) 2D RCE simulation over 300 K. Appendix A shows the evolution of the self-aggregated convection filtered for its band within the dashed box in the top row of Figure 2. With increasing system rotation rate (from top to bottom of Figure 2), the spectra seem similar, but the gravity wave peaks shift with the dispersion lines (both dotted and solid) significantly in the X64 spectra (bottom row of Figure 2).

We compare Figure 2 with the raw observed power spectra of eastward propagating convection symmetric about the equator (Figure 1 of Roundy 2020; see also Kiladis et al. 2009; WK99). When convectively coupled, the simulated gravity waves (dotted lines in Figure 2) as well as the observed Kelvin waves (e.g., Figure 3b of WK99) correspond to an equivalent depth of about 25 m. However, unlike the raw simulation spectra with multiple maxima in frequency (Figure 2), the raw observational spectra do not show a peak in the Kelvin wave band. Instead,

the Kelvin wave maximum emerges from the normalization by a smoothed background spectrum (Roundy 2020). Another notable difference lies in the horizontal scale of the low-frequency power maxima; the simulated convective clusters scale ~ 2,000 km while the MJO scales ~ 20,000 km.

We expect that the CBE introduces asymmetry to the power spectra. Supposedly, the CBE tends to shift eastward power to a faster band and westward power to a slower band. To test this hypothesis, we first contrast the X64 spectra to the symmetric X00 spectra (bottom row of Figure 3; Section 3b). First, the precipitation spectrum (Figure 2a) shows bands where the power gradient directs against the dispersion line rotation due to the CBE (Figure 1), including the counterclockwise side of the dotted lines, the clockwise side of the solid lines, and a band roughly covering wavenumber from 6 to 14 and period of 7 days or longer. In these bands, the spectral power increases in the X64 spectrum (Figure 3i) as if the CBE shifts the power down its gradient. Similarly, in the USFC spectrum (Figure 2c), such down-gradient power shift due to the CBE occurs in bands including the counterclockwise side of the dotted and solid lines as well as a part of the self-aggregated convection band roughly within wavenumber 2 and 14 along with its extension toward the dotted line. The power also increases in these bands in the X64 spectrum (Figure 3k). On the other hand, the power generally decreases in these spectra (Figure 3i and 3k) in bands with up-gradient power shift due to the CBE. Similar reasoning applies to the PW (Figure 3j) and U200 (Figure 3l) spectra except the upward side of the dispersion lines in the PW spectrum, which implies power changes in a non-shifting manner. With decreasing system rotation rate (from bottom to top of Figure 3), the power ratio becomes noisy, but the above-mentioned power changes can mostly be found to have small magnitude. Despite these caveats, the CBE theory makes useful explanations for the spectral changes due

197 to the inclusion of NCTs, which tends to shift eastward power to a faster band and westward
198 power to a slower band.

199 To quantitatively test the FOCBE theory, we first estimate the FOCBE parameter. The
200 simulations and the observations yield different vertical-mode spectra of kinetic energy; the
201 former peak at the third mode, but the latter peak at the first mode (Figure 4). Unlike the
202 observational red spectrum with a concentrated single maximum, the simulation spectra are
203 characterized by not only the prominent third-mode peak but also weaker redness with energy
204 dispersed into higher vertical modes (Figure 4). Besides, the power slightly moves from the
205 first two modes to higher when filtered for the timescale of simulated gravity waves (1.5 to 18
206 days in Figure 2) and observed Kelvin waves (2.5 to 30 days in WK99). With these caveats,
207 the most energetic vertical mode is taken to estimate the characteristic FOCBE parameter of
208 the observation and each simulation (Table 1).

209 Finally, we test the FOCBE theory quantitatively. To avoid complication due to the
210 proximity of the two types of gravity wave peaks, we measure the gravity wave speed from the
211 normalized precipitation spectra (Figure 5a column), where the dry gravity wave peaks are
212 absent. The measured gravity wave speed (solid lines) captures the gravity wave peaks in the
213 normalized spectra of the other variables (Figure 5). As a caveat, the smoothed background
214 spectra for the normalization also change with the system rotation rate. Nevertheless, our
215 conclusion holds even when measuring the gravity wave speed from the raw spectra. We take
216 the average of the positive and negative phase speed as the speed change (Δc).

217 The Δc results (Figure 6) agree with their FOCBE parameter (Table 1). The X00 results are
218 about zero and not shown in Figure 6 because they include negative values, which cannot be
219 converted to log scale. The X01 results are uncertain because of a lack of the resolution. The
220 other simulation results are incremental to c (about 16 m s^{-1}) and discernable by computers but

maybe not by eyes except that the X64 results yield Δc scaling 12% of c, which is noticeable by sight (bottom row of Figures 2, 3, and 5). Nevertheless, the robust agreement shown in Figure 6 confirms that the dry-dynamical FOCBE theory can predict Δc due to the inclusion of NCTs even given the free interactions between circulation and moist physics in the 2D RCE.

5. Summaries and Discussions

This study explores effects of the nontraditional Coriolis terms (NCTs) on explicitly simulated convective system propagation in radiative-convective equilibrium (RCE) in a zonal vertical domain using the System for Atmospheric Modeling (SAM). We restored NCTs to SAM to represent the effects of system rotation about a meridional axis. The system rotation rate is tested over a wide range. We hypothesize that the inclusion of NCTs speeds up the eastward propagation and slows down the westward propagation because the first-order compressional beta effect (FOCBE) tends to transmit zonal vertical circulation eastward. The simulated propagation characteristics are analyzed with space-time spectra. The raw spectra show local power maxima in bands associated with self-aggregated convection and convectively coupled gravity waves. The CBE can qualitatively explain the spectral power increase in the band of eastward propagating convective clusters and its decrease in the band of westward ones. Furthermore, this study measures the speed change of convectively coupled gravity waves from the precipitation spectra. The resulting speed change agrees with the theoretical speed change due to the FOCBE, which is estimated from the system rotation rate, the scale height, and the vertical wavenumber derived from the vertical-mode analysis. These changes due to the inclusion of NCTs are robust and considerable to a far larger extent than the computational cost for the implementation of NCTs in SAM of less than 0.01%. Thus, the restoration of NCTs is economical for model development, which reconfirms previous studies

restoring NCTs to global atmospheric dynamical cores using the quasi-hydrostatic equations (White and Bromley 1995) or the fully nonhydrostatic equations (e.g., Skamarock et al. 2021).

The results may have implications for the propagation speed of the MJO. The FOCBE can be easily introduced to two of the diverse MJO theories. First, Yang and Ingersoll (2013) determined the MJO speed by the average of inertio-gravity wave speed (negative westward and vice versa), which may increase by one FOCBE parameter. Second, Kim and Zhang (2021) proposed that the MJO speed arises from the damped Kelvin wave speed, which may speed up by one FOCBE parameter. Given the FOCBE parameter of the first vertical mode from the Merged Sounding during DYNAMO (Table 1), these two theories imply that the FOCBE contributes 0.265 m s^{-1} to the eastward propagation of the MJO (the largest blue star mark in Figure 6). Supposedly, the FOCBE contributes 3% to 13% to the MJO speed ranging from 8 to 2 m s^{-1}. For example, for slow MJO episodes that propagate from 90°E to 160°E in 40 days (see a composite in Figure 4 of Yadav and Straus 2017), the omission of NCTs may delay the arrival by 5 days. However, given the diversity of MJO theories (Zhang et al. 2020), further studies are needed.

Our results show that NCTs can produce a significant east-west asymmetry in the spectral power density of precipitation, PW, and winds. The asymmetry can lead to enhanced power of low frequency variability of eastward propagating signals (e.g., Figure 3f and 3j), which are associated with convective self-aggregation in our simulations and might become the MJO in the real atmosphere. Therefore, restoring NCTs in atmospheric models may improve the representation of the MJO, the variability of which is significantly underestimated by the current climate models (Le et al. 2021).

Acknowledgments.

This research is supported by a Packard Fellowship awarded to D.Y.

Data Availability Statement.

We thank the German Climate Computing Center (DKRZ) for hosting the standardized RCEMIP data, which is publicly available at https://hdl.handle.net/21.14101/d4beee8e-6996-453e-bbd1-ff53b6874c0e. The Merged Sounding data were obtained from the Atmospheric Radiation Measurement (ARM) Program sponsored by the U.S. Department of Energy, Office of Science, Office of Biological and Environmental Research, Climate and Environmental Sciences Division via doi:10.5439/1034922 with free registration. The model, SAM, can be used only with permission from Marat Khairoutdinov (marat.khairoutdinov@stonybrook.edu).

APPENDIX

Appendix A: Filtering for the Self-Aggregated Convection

To confirm the association of the self-aggregated convection with the spectral band in the dashed box in the top row of Figure 2, the PW is filtered for this band. The Hovmöller diagrams of the filtered PW (Figure A1) show many convective clusters (solid contours) and dry regions (dashed contours). These systems grow (or split), migrate, and decay (or merge) in a complex manner with generally 12 convective clusters maintained in total. Such metabolism occurs in periods other than the 96 days shown in Figure A1.

REFERENCES

Eckart, C., 1960: *Hydrodynamics of Oceans and Atmospheres.* Pergamon Press, 290 pp, https://doi.org/10.1016/C2013-0-01648-9.

Fulton, S. R., and W. H. Schubert, 1985: Vertical normal mode transforms: Theory and application. *Mon. Wea. Rev.*, **113,** 647–658, https://doi.org/10.1175/1520-0493(1985)113<0647:VNMTTA>2.0.CO;2.

Giangrande, S., G. Mace, and D. Turner, 2011: Merged Sounding (MERGESONDE1MACE). Atmospheric Radiation Measurement (ARM) user facility, accessed 4 April 2021, https://doi.org/10.5439/1034922.

Gilman, P. A., and G. A. Glatzmaier, 1981: Compressible convection in a rotating spherical shell. I-Anelastic equations. II-A linear anelastic model. III-Analytic model for compressible vorticity waves. *Astrophys. J. Suppl. Ser.*, **45,** 335–388, https://doi.org/10.1086/190714.

Glatzmaier, G. A., M. Evonuk, and T. M. Rogers, 2009: Differential rotation in giant planets maintained by density-stratified turbulent convection. *Geophys. Astrophys. Fluid Dyn.*, **103,** 31–51, https://doi.org/10.1080/03091920802221245.

Hayashi, M., and H. Itoh, 2012: The importance of the nontraditional Coriolis terms in large-scale motions in the tropics forced by prescribed cumulus heating. *J. Atmos. Sci.*, **69,** 2699–2716, https://doi.org/10.1175/JAS-D-11-0334.1.

Hayashi, Y., 1971: A generalized method of resolving disturbances into progressive and retrogressive waves by space Fourier and time cross-spectral analyses. *J. Meteor. Soc. Japan*, **49,** 125–128, https://doi.org/10.2151/jmsj1965.49.2_125.

——, 1982: Space-time spectral analysis and its applications to atmospheric waves. *J. Meteor. Soc. Japan*, **60,** 156–171, https://doi.org/10.2151/jmsj1965.60.1_156.

Held, I. M., R. S. Hemler, and V. Ramaswamy, 1993: Radiative-convective equilibrium with explicit two-dimensional moist convection. *J. Atmos. Sci.*, **50,** 3909–3927, https://doi.org/10.1175/1520-0469(1993)050<3909:RCEWET>2.0.CO;2.

Igel, M. R., and J. A. Biello, 2020: The nontraditional Coriolis terms and tropical convective clouds. *J. Atmos. Sci.*, **77,** 3985–3998, https://doi.org/10.1175/JAS-D-20-0024.1.

313 Khairoutdinov, M. F., and D. A. Randall, 2003: Cloud resolving modeling of the ARM
314 summer 1997 IOP: Model formulation, results, uncertainties, and sensitivities. *J. Atmos.*
315 *Sci.*, **60,** 607–625, https://doi.org/10.1175/1520-
316 0469(2003)060<0607:CRMOTA>2.0.CO;2.

317 Kiladis, G. N., M. C. Wheeler, P. T. Haertel, K. H. Straub, and P. E. Roundy, 2009:
318 Convectively coupled equatorial waves. *Rev. Geophys.*, **47**, RG2003,
319 https://doi.org/10.1029/2008RG000266.

320 Kim, J.-E., and C. Zhang, 2021: Core dynamics of the MJO. *J. Atmos. Sci.*, **78,** 229–248,
321 https://doi.org/10.1175/JAS-D-20-0193.1.

322 Le, P. V., C. Guilloteau, A. Mamalakis, and E. Foufoula-Georgiou, 2021: Underestimated
323 MJO variability in CMIP6 models. *Geophys. Res. Lett.*, **48,** e2020GL092244,
324 https://doi.org/10.1029/2020GL092244.

325 Matsuno, T., 1966: Quasi-geostrophic motions in the equatorial area. *J. Meteor. Soc. Japan*,
326 **44,** 25–43, https://doi.org/10.2151/jmsj1965.44.1_25.

327 Ong, H., and P. E. Roundy, 2019: Linear effects of nontraditional Coriolis terms on
328 intertropical convergence zone forced large-scale flow. *Quart. J. Roy. Meteor. Soc.*, **145,**
329 2445–2453, https://doi.org/10.1002/qj.3572.

330 ——, and ——, 2020a: Nontraditional hypsometric equation. *Quart. J. Roy. Meteor. Soc.*,
331 **146,** 700–706, https://doi.org/10.1002/qj.3703.

332 ——, and ——, 2020b: The compressional beta effect: Analytical solution, numerical
333 benchmark, and data analysis. *J. Atmos. Sci.*, **77,** 3721–3732,
334 https://doi.org/10.1175/JAS-D-20-0124.1.

Roundy, P. E., 2020: Interpretation of the spectrum of eastward-moving tropical convective anomalies. *Quart. J. Roy. Meteor. Soc.*, **146,** 795–806, https://doi.org/10.1002/qj.3709.

Skamarock, W. C., H. Ong, and J. B. Klemp, 2021: A fully compressible nonhydrostatic deep-atmosphere equations solver for MPAS. *Mon. Wea. Rev.*, **149,** 571–583, https://doi.org/10.1175/MWR-D-20-0286.1.

Vallis, G. K., 2017: *Atmospheric and Oceanic Fluid Dynamics.* Cambridge University Press, 946 pp., https://doi.org/10.1017/9781107588417.

Verhoeven, J., and S. Stellmach, 2014: The compressional beta effect: A source of zonal winds in planets? *Icarus*, **237,** 143–158, https://doi.org/10.1016/j.icarus.2014.04.019.

Wheeler, M., and G. N. Kiladis, 1999: Convectively coupled equatorial waves: Analysis of clouds and temperature in the wavenumber–frequency domain. *J. Atmos. Sci.*, **56,** 374–399, https://doi.org/10.1175/1520-0469(1999)056<0374:CCEWAO>2.0.CO;2.

White, A. A., and R. Bromley, 1995: Dynamically consistent, quasi-hydrostatic equations for global models with a complete representation of the Coriolis force. *Quart. J. Roy. Meteor. Soc.*, **121,** 399–418, https://doi.org/10.1002/qj.49712152208.

Wing, A. A., K. A. Reed, M. Satoh, B. Stevens, S. Bony, and T. Ohno, 2018: Radiative–convective equilibrium model intercomparison project. *Geosci. Model Dev.*, **11,** 793–813, https://doi.org/10.5194/gmd-11-793-2018.

——, and Coauthors, 2020: Clouds and convective self-aggregation in a multimodel ensemble of radiative-convective equilibrium simulations. *J. Adv. Model. Earth Syst.*, **12,** e2020MS002138, https://doi.org/10.1029/2020MS002138.

Yadav, P., and D. M. Straus, 2017: Circulation response to fast and slow MJO episodes. *Mon. Wea. Rev.*, **145,** 1577–1596, https://doi.org/10.1175/MWR-D-16-0352.1.

Yang, D., 2018: Boundary layer height and buoyancy determine the horizontal scale of convective self-aggregation. *J. Atmos. Sci.*, **75,** 469–478, https://doi.org/10.1175/JAS-D-17-0150.1.

——, and A. P. Ingersoll, 2013: Triggered convection, gravity waves, and the MJO: A shallow-water model. *J. Atmos. Sci.*, **70,** 2476–2486, https://doi.org/10.1029/2017MS001261.

Yoneyama, K., C. Zhang, and C. N. Long, 2013: Tracking pulses of the Madden–Julian oscillation. *Bull. Amer. Meteor. Soc.*, **94,** 1871–1891, https://doi.org/10.1175/BAMS-D-12-00157.1.

Zhang, C., Á. Adames, B. Khouider, B. Wang, and D. Yang, 2020: Four Theories of the Madden-Julian Oscillation. *Rev. Geophys.*, **58,** e2019RG000685, https://doi.org/10.1029/2019RG000685.

370 TABLES

371 **Table 1**. The Characteristic FOCBE Parameter

Case name	Ω[1]	M	D (km)	H (km)[2]	FOCBE (m s^{-1})
DYNAMO	1	1	17.0	7.0	0.265
X00	0	3	15.5	7.0	0
X01	1	3	15.5	7.0	0.028
X04	4	3	15.5	7.0	0.111
X08	8	3	15.5	7.0	0.222
X16	16	3	15.5	7.0	0.445
X64	64	3	15.5	7.0	1.779

372

[1]Normalized by the Earth's rotation rate of 7.292×10^{-5} s^{-1}.

[2]Virtual temperature times gas constant divided by gravity acceleration averaged in the troposphere with the data equally spaced in height.

373 FIGURES

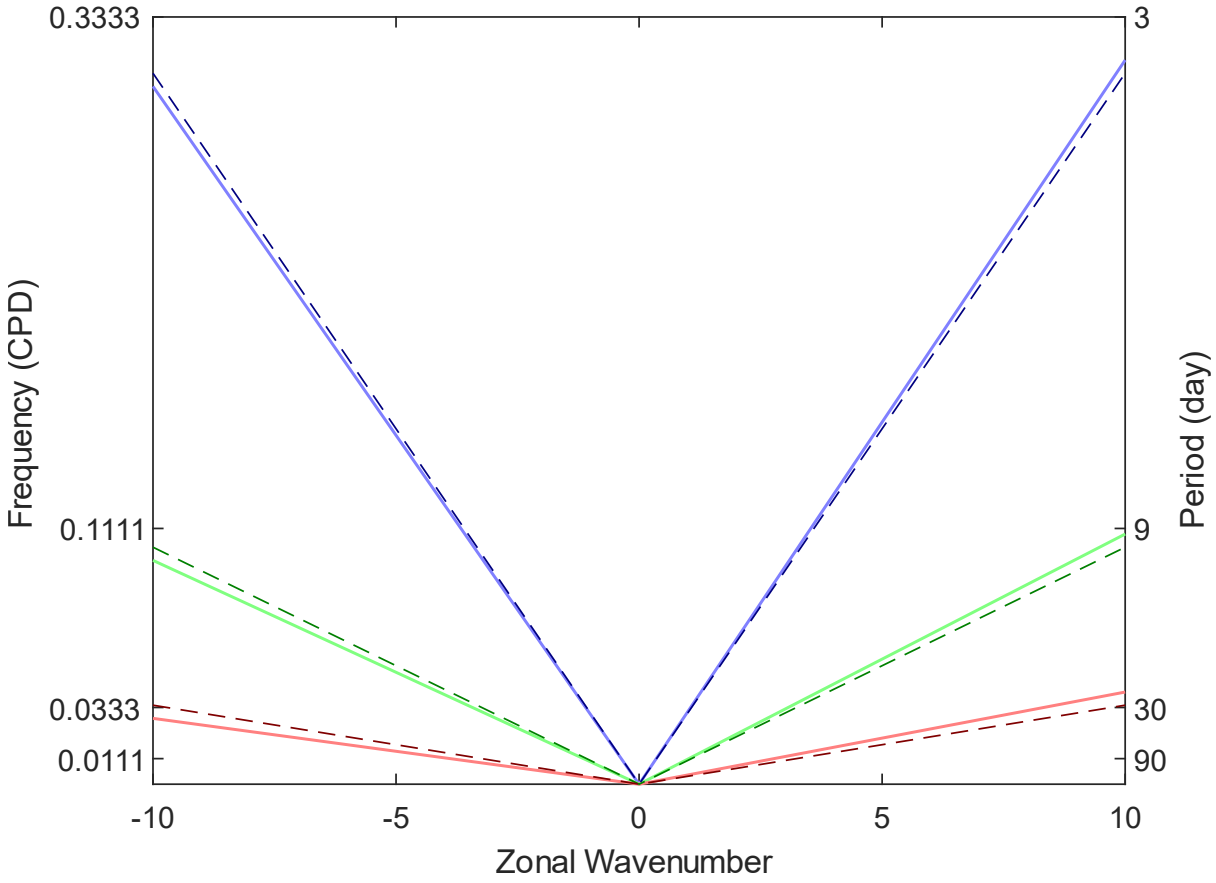

374

375 **Figure 1**. Zonal temporal dispersion relations of gravity waves confined to a zonal vertical
376 plane at the equator with the FOCBE parameter of 0.265 m s^{-1} (solid) and without the FOCBE
377 (dash). The red, green, and blue lines correspond to $\hat{\Omega}$ of 1/6, 1/18, and 1/54.

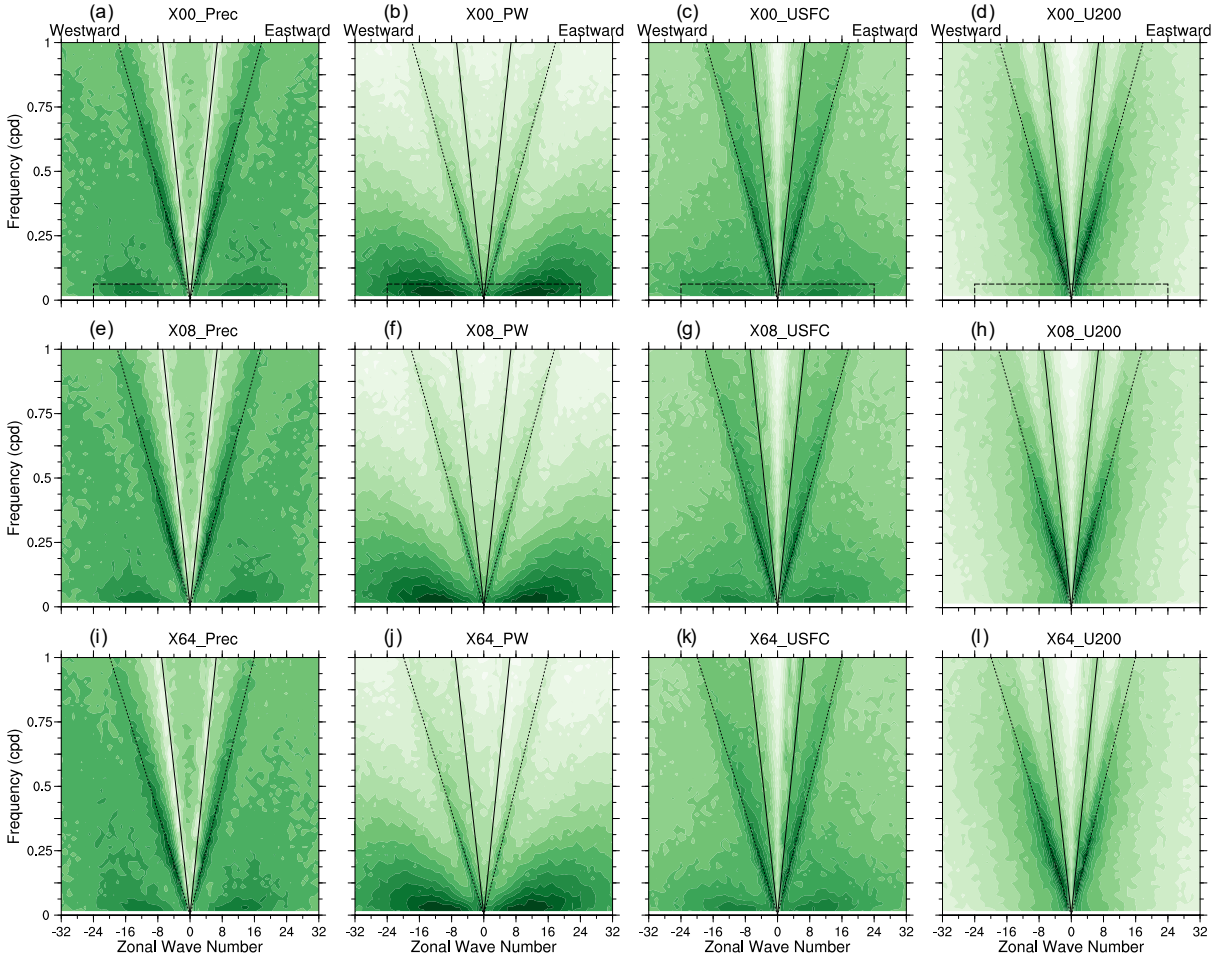

Figure 2. Raw spectra of (from left to right) the precipitation rate, precipitable water, zonal velocity at the lowest level and at 200 hPa from (from top to bottom) the X00, X08, and X64 simulations. The darker shading denotes the larger base-10 logarithm of the power; the shading interval is 0.3 arbitrary units. The superimposed lines are cited in text.

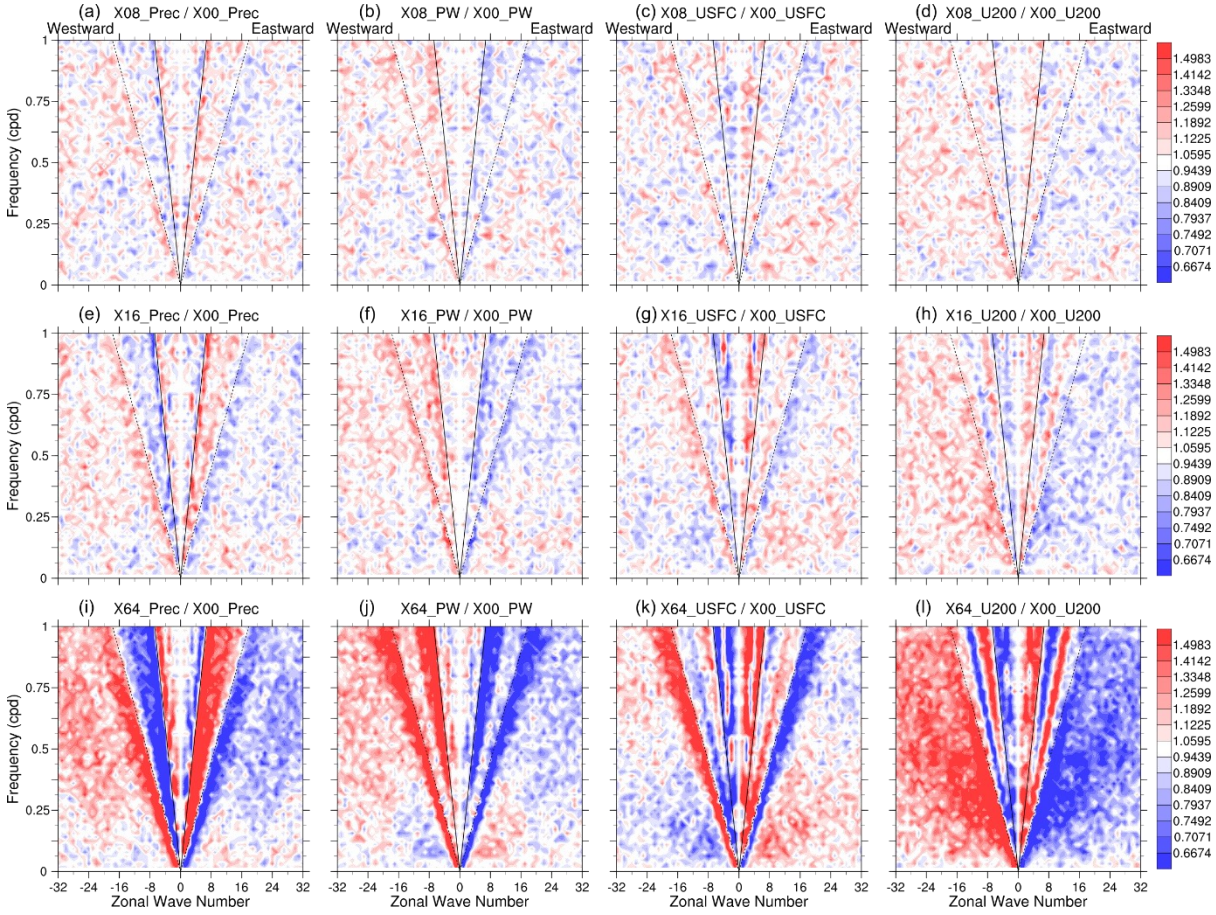

Figure 3. Like Figure 2, but the shading denotes the power ratio of the X08, X16, and X64 to the symmetrized X00. The shading levels are spaced by a common ratio of $\sqrt[12]{2}$ (like a semitone of an equally tempered musical instrument) except that the level 1 is omitted.

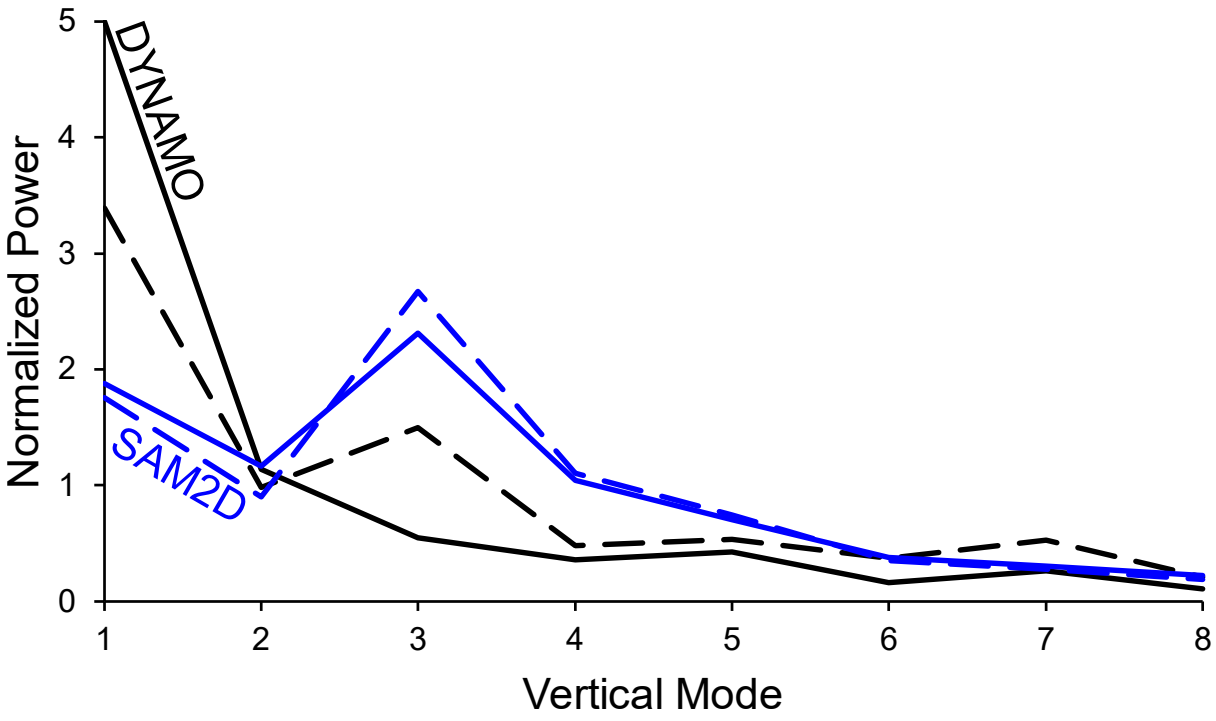

Figure 4. Vertical-mode spectra of kinetic energy (power) derived from zonal velocity profiles in the Merged Sounding during DYNAMO (black) and the 2D RCE with SAM (blue), each unfiltered (solid) and filtered for the timescale of Kelvin or gravity waves (dashed, see text). The power is normalized by the average in the first eight modes.

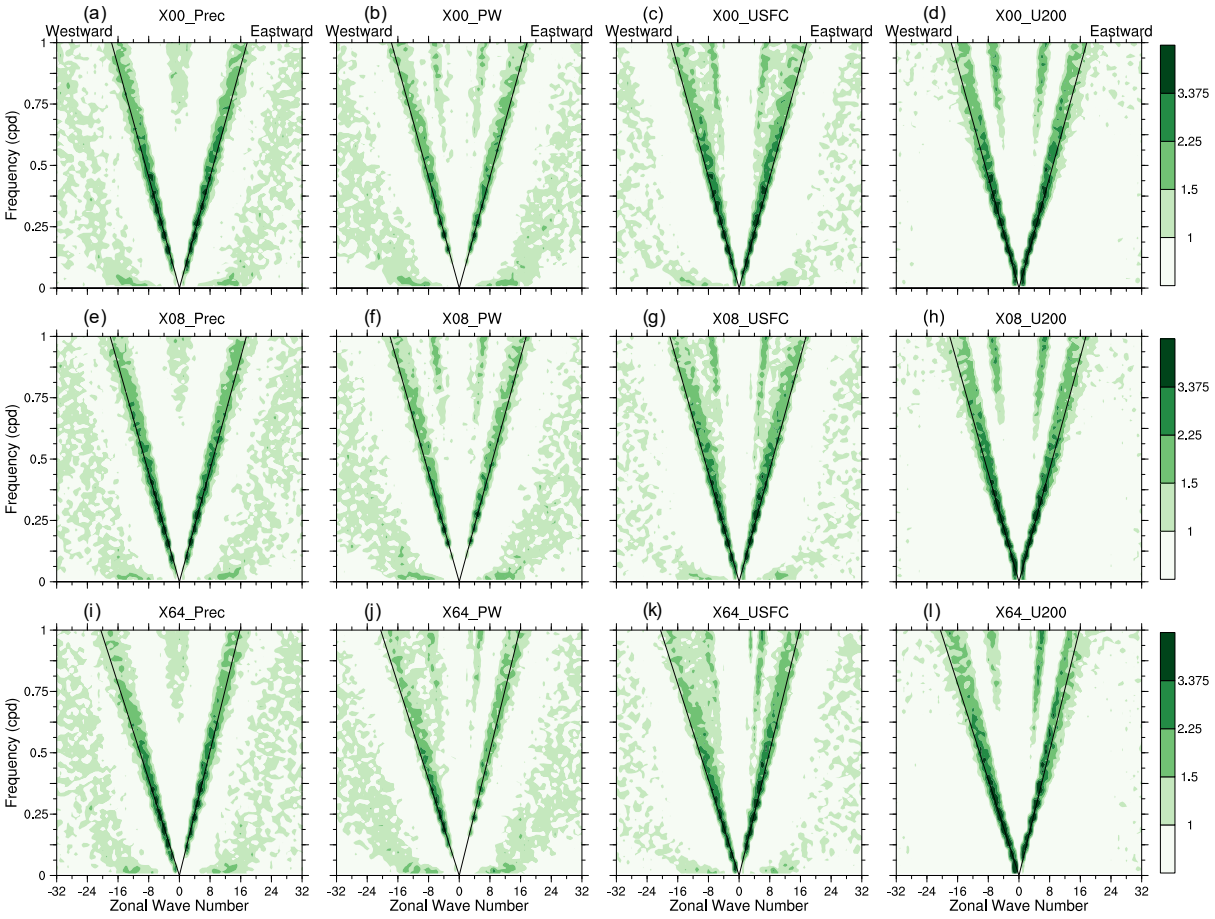

Figure 5. Like Figure 2 but depicting the ratio of the raw spectrum to the background spectrum. The sample length is set to 128 days, and the background is smoothed for 64 times in wavenumber.

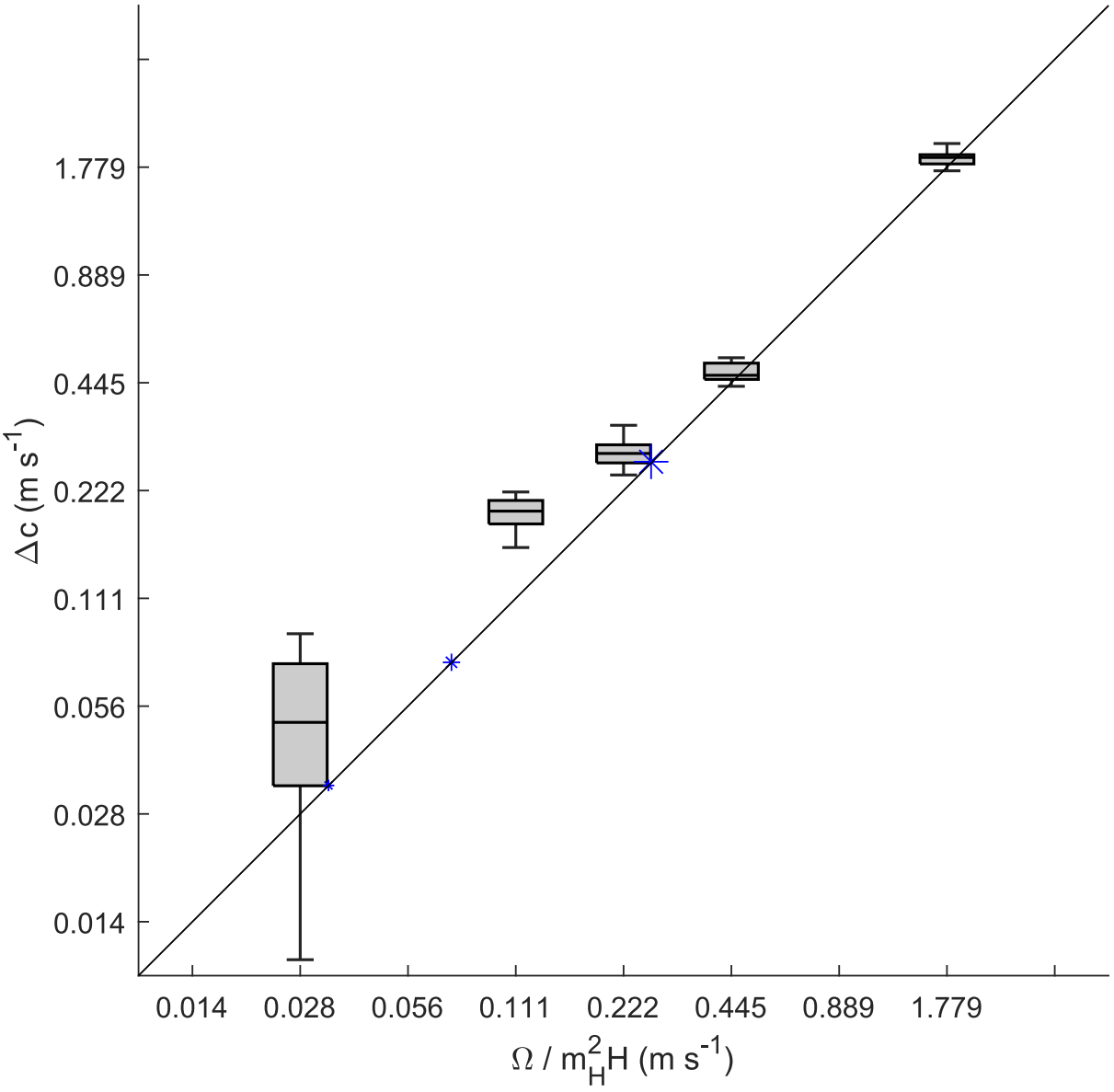

396

397 **Figure 6**. Scaling of the gravity wave speed change (boxes and whiskers) against the FOCBE
398 parameter (horizontal axis, see Table 1). Each box-whiskers set denotes the quartiles and full
399 range of the speed measurement results from each simulation. The blue star marks denote the
400 first, second, and third vertical modes (from right to left) from the Merged Sounding during
401 DYNAMO; the mark sizes are proportional to the unfiltered power. The axes are log scaled.

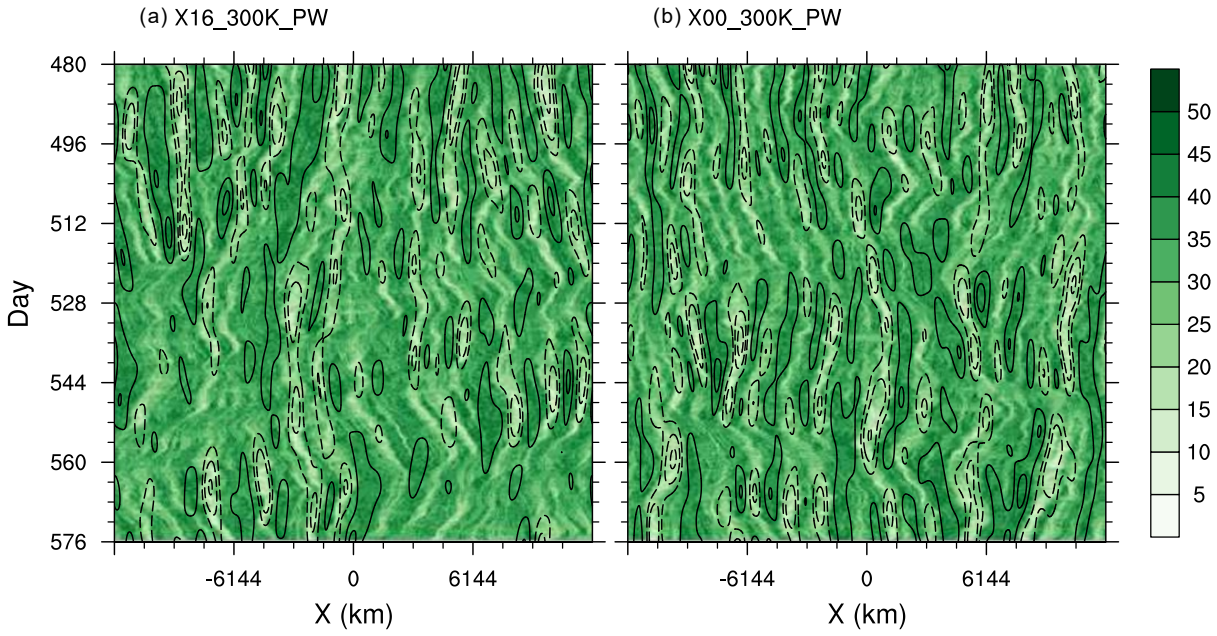

Figure A1. Hovmöller diagrams of the PW in the 2D RCE (a) with NCTs (X16) and (b) without NCTs from the raw data (shading, mm) and data filtered for the self-aggregated convection (contours, interval: 5 mm). The solid and dashed contours denote positive and negative values, and the zero contour is omitted.